Available online at www.sciencedirect.com
ScienceDirect
Acta Materialia 59 (2011) 5224–5237
Acta MATERIALIA
www.elsevier.com/locate/actamat

Microstructural evolution and creep properties of precipitation-strengthened Al–0.06Sc–0.02Gd and Al–0.06Sc–0.02Yb (at.%) alloys

Marsha E. Van Dalen [a,1], David C. Dunand [a,*], David N. Seidman [a,b]

[a] Department of Materials Science and Engineering, Northwestern University, 2220 Campus Dr., Evanston, IL 60208-3108, USA
[b] Northwestern University Center for Atom-Probe Tomography (NUCAPT), Northwestern University, 2220 Campus Dr., Evanston, IL 60208-3108, USA

Received 22 March 2011; received in revised form 24 April 2011; accepted 25 April 2011
Available online 27 May 2011

Abstract

The aging behavior at 300 °C of Al–0.06Sc–0.02Gd and Al–0.06Sc–0.02Yb (at.%) alloys is studied by local-electrode atom-probe tomography, transmission electron microscopy and microhardness measurements. The ternary alloys exhibit high number densities of coherent $L1_2$ precipitates ($N_v \cong 10^{22}$ m^{-3}) at aging times up to 1536 h (64 days). In the Al–0.06Sc–0.02Gd alloy, the $Al_3(Sc_{1-x}Gd_x)$ precipitates are always Sc-rich, displaying a small Gd concentration ($x < 0.12$) in the precipitates. In the Al–0.06Sc–0.02Yb alloy, the precipitates are initially Yb-rich, $Al_3(Yb_{1-x}Sc_x)$, with Sc diffusing subsequently to the precipitates, resulting in a core/shell structure and an overall Sc-rich composition, $Al_3(Sc_{1-x}Yb_x)$. Gd and Yb, like other lanthanides but unlike the transition metals Zr and Ti, do not retard the coarsening kinetics compared with binary Al–Sc alloys. Additionally, the creep resistance of these alloys is greater than that of Al–Sc alloys. The coarsening kinetics and creep properties of Al–0.06Sc–0.02Gd and Al–0.06Sc–0.02Yb alloys are compared with other Al–Sc-based alloys and with coarsening models for ternary alloys.

Keywords: Aluminum alloys; Nucleation; Precipitation; Coarsening; Creep

1. Introduction

Cast, dilute Al–Sc-based alloys exhibit promising creep resistance at 300 °C (61% of the absolute melting point of aluminum) [1]. A coarse-grained matrix (grain diameter ~1 mm), which is favorable for creep resistance, forms upon homogenization of these alloys in the single-phase α-Al region [1], which has a maximum solubility of 0.23 at.% (0.38 wt.%) Sc at the eutectic temperature of 660 °C [2–6]. After quenching from the α-Al solid-solution phase-field, homogeneously distributed precipitates are observed upon aging in the α-Al + Al_3Sc($L1_2$ structure) phase-field, with continuous precipitation observed up to ~350 °C [3,7]. These aged, coarse-grained alloys display high creep resistance [1,8–11], owing to the formation of a high number density ($N_v \sim 10^{22}$ m^{-3}) of nanoscale Al_3Sc precipitates with the $L1_2$ structure, with no intermediate metastable phases forming. The Al_3Sc precipitates remain coherent to diameters of ~40 nm [12,13], owing to a relatively small lattice-parameter mismatch between the Al_3Sc precipitates and the α-Al matrix ($\delta = 1.1\%$ at 300 °C) [14,15]. In binary Al–Sc alloys, the precipitate radii $\langle R \rangle$ coarsen with a $\sim t^{1/3}$ dependence, which is predicted for diffusion-limited coarsening [1,5,11,13,16–18].

The effects of ternary additions to dilute Al–Sc alloys have been investigated with the goal of improving both coarsening and creep resistance of coarse-grained Al–Sc alloys. Magnesium additions to Al–Sc alloys lead to solid-solution strengthening of the α-Al matrix with very little Mg incorporation into the Al_3Sc precipitates [10]: Mg is insoluble in Al_3Sc. Lithium additions, in contrast,

* Corresponding author. Tel.: +1 847 491 5370.
E-mail address: dunand@northwestern.edu (D.C. Dunand).
[1] Present address: Momentive Performance Materials, 24400 Highland Rd., Richmond Heights, OH 44143, USA.

1359-6454/$36.00 © 2011 Acta Materialia Inc. Published by Elsevier Ltd. All rights reserved.
doi:10.1016/j.actamat.2011.04.059

provide solid-solution strengthening and, through incorporation of Li in the $Al_3(Sc_{1-x}Li_x)$ precipitates, increase their volume fraction and number density, while reducing their precipitate radii [19]. Adding zirconium to dilute Al–Sc alloys results in partitioning of Zr to the Al_3Sc precipitates forming $Al_3(Sc_{1-x}Zr_x)$ precipitates, which exhibit much improved stability and coarsening resistance at 300 °C [20,21]. In the bulk $Al_3(Sc,Zr)$ intermetallic phase, Zr can replace up to 50% of the Sc ($x = 0.5$), while retaining the $L1_2$ structure [14,22,23]. Since Zr is significantly less expensive than Sc, the same precipitate volume fraction, ϕ, can be achieved while employing less Sc. In Al–Sc–Zr alloys, the Zr in the precipitates is found to be well below its solubility limit [21,24–26], because the small diffusivity of Zr in Al limits the diffusive flux of Zr to the precipitates [27]. Lattice kinetic Monte Carlo (LKMC) simulations demonstrate that the Zr segregates at the α-Al/Al_3Sc interface, forming a Zr-enriched spherical shell [28,29], which is in agreement with earlier experiments [9,20,23–26,28,30]. Titanium, another slow diffuser in Al, has a similar effect to Zr [31]: it decreases the coarsening kinetics and segregates at the Al/$Al_3(Sc_{1-x}Ti_x)$ interface forming a Ti-enriched shell [32]. Again, owing to the small diffusivity of Ti in Al, only a small concentration of Ti is incorporated in the precipitates, e.g., 1.5% after 64 days of aging at 300 °C. In contrast, for an Al–Li–Zr alloy, the coarsening kinetics of the core/shell precipitates are not decelerated in the temperature range 170–230 °C [33]. In this case, Zr resides in the precipitates' cores with a Li-rich $Al_3(Li_{1-x}Zr_x)$ shell [33].

Rare-earth (RE) elements are attractive ternary additions to Al–Sc alloys for different reasons [34]. First, many RE elements have a high solubility in Al_3Sc precipitates, substituting for Sc and forming $Al_3(Sc_{1-x}RE_x)$ precipitates, thereby replacing the more expensive Sc [35–37]. For the four heaviest RE, including Er [38] and Yb [36], the solubility reaches 100% (expressed as a percentage of Sc replaced in $L1_2$ precipitates), since these elements form $Al_3RE(L1_2)$ precipitates [37]. For some of the lighter RE, the solubilities in Al_3Sc are small, for example, 12 and 15 at.% for Sm [39] and Gd [35], respectively, which is related to the non-$L1_2$ structure of Al_3Sm and Al_3Gd [40]. Secondly, the light RE (La through Sm) have smaller diffusivity in Al than does Sc [41], thereby improving the coarsening resistance of the precipitates, but they have a larger diffusivities in Al [41] than do the transition metals Ti, Zr or Hf [32], and therefore the RE are incorporated into the $L1_2$ precipitates to a larger extent than these transition metals. Some of the heavier RE have larger diffusivities in Al compared with Sc [42]. Finally, unlike Ti, Zr or Hf [14], RE increase the lattice parameter mismatch between α-Al and $Al_3(Sc_{1-x},RE_x)$ [35–37], which can increase the creep resistance [43]. Similar to Sc, the solubility of the RE in α-Al is very limited and thus the maximum attainable volume fraction, ϕ, of precipitates is small, although the exact solubility for most RE at 300 °C is unknown, with the exception of Gd, Er and Yb [42,44].

Sawtell and Morris investigated Y, Gd, Ho and Er as alloying additions to hypereutectic Al–0.3 at.% Sc [45], while others have studied RE additions to Al alloys both with and without Sc additions [46–52]. The present authors' studies [19,53–57] have focused on dilute Al–Sc–RE alloys, which upon aging exhibit a precipitate number density greater than in binary Al–Sc alloys [12] with similar volume fractions ($\phi = 0.25$–0.50%). The present article examines in detail the coarsening and creep properties of dilute Al–Sc alloys containing Gd or Yb. The coarsening kinetics and creep properties of Al–Sc–Gd and Al–Sc–Yb (at.%) alloys are compared with other Al–Sc-based alloys and with coarsening models for ternary alloys.

2. Experimental methods

Alloy compositions, as verified by ATI Wah Chang (Albany, OR), were Al–0.061 ± 0.003Sc–0.018 ± 0.009Gd (hereafter referred to as Al–Sc–Gd) and Al–0.058 ± 0.003Sc–0.024 ± 0.008Yb (hereafter referred to as Al–Sc–Yb): all compositions are in at.% unless otherwise noted. To increase the probability that each alloy was in the α-Al phase field during homogenization, the Sc concentration was maintained well below the maximum Sc solubility of 0.23 at.% in Al–Sc, while that of Yb is below the maximum Yb solubility of 0.025 at.% at 625 °C in binary Al–Yb [42]: note the large differences between the Sc and Yb solubilities in Al. The Gd solubility in Al–Gd is unknown, but is probably similar to that of Yb (0.025 at.% at 640 °C) [42] and other RE [42,44,58,59]. Each alloy was produced by dilution casting, using Al–1.2 wt.% Sc (Ashurst) and Al–2 wt.% RE (Stanford Materials) master alloys with 99.99 wt.% pure Al (the main impurities are 22 ± 3 at.ppm Fe and 38 ± 5 at.ppm Si). The alloys were melted in an alumina crucible in a resistively heated furnace at 750 °C in air. After thorough stirring, the melt was cast into a graphite mold resting on a large copper platen and cooled to ambient temperature. Homogenization was then performed at 640 °C for 24 h in air and terminated by water quenching to room temperature. Subsequent aging at 300 °C (also terminated by water quenching) was performed in air, except for samples aged for less than 15 min, which were aged in a molten mixture of sodium nitrite, sodium nitrate and potassium nitrate.

Vickers microhardness measurements were performed with a 200 g weight at room temperature on samples ground to a 1 μm surface finish; ten measurements were recorded on each sample. Transmission electron microscopy (TEM) was performed using a Hitachi 8100 microscope operating at 200 kV. TEM foils were mechanically ground to a thickness of 200 μm and subsequently electropolished using a Struers Tenupol-5 in a solution of 5 vol.% perchloric acid in methanol at −20 °C, which was cooled in a bath of dry ice in methanol.

Sample blanks for atom-probe tomography (APT) were produced by mechanically grinding material to a square

cross-sectional area of ~300 × 300 μm^2. The samples were then electropolished using a two-stage procedure. The initial polishing was performed using a solution of 10 vol.% perchloric acid in acetic acid, and the final polishing was performed using a solution of 2 vol.% perchloric acid in butoxyethanol. Experiments were performed employing a Cameca (formerly Imago Scientific Instruments, Madison, WI) local-electrode atom-probe (LEAP) tomograph [60,61]. The local-electrode produces an enhanced electric-field compared with standard APT [60,62]. The data were collected using the electrical pulsing mode at 30 K at a pulse repetition rate of 200 kHz. Proximity histogram plots [63] were calculated employing ADAM or APEX software [64] using an isoconcentration surface of 9 at.% Sc. A total of 10–100 precipitates were analyzed for each aging time using LEAP tomography.

The creep samples were pre-aged to produce precipitates with a particular radius. These aging treatments were: 24 h at 300 °C (2.9 nm for Al–Sc–Yb and 2.4 nm for Al–Sc–Gd), 384 h at 300 °C (4.0 nm for Al–Sc–Yb and 3.6 nm for Al–Sc–Gd) and a double aging treatment: 24 h at 300 °C followed by 24 h at 400 °C (29 nm for Al–Sc–Yb and 19.7 nm for Al–Sc–Gd). To ensure a uniform temperature during creep testing, the samples were allowed to soak at the testing temperature for 2 h prior to loading. Creep experiments were performed in a nickel-based superalloy compression cage, and the sample ends were lubricated with boron nitride to reduce friction between the cage and the sample. The displacement was measured with a linear variable differential transducer connected to an extensometer. Sufficient time was allowed to achieve a minimum strain rate for each successively higher load applied to the sample. The creep experiments were terminated when a sample achieved a total strain of 10%. No sample was crept for more than 10 days to ensure that the precipitates did not coarsen significantly during an experiment (according to the coarsening experiments at 300 °C, the precipitate radii would be increased by a maximum of 1 nm during that time frame). The minimum strain rates were observed at multiple stresses for each sample. The stress was always increased, since there is a change in the dislocation density with increasing stress.

3. Experimental results

3.1. Microhardness

Fig. 1 displays the Vickers microhardness for Al–Sc–Yb and Al–Sc–Gd alloys as a function of aging time at 300 °C [53]. The alloys achieve peak Vickers microhardness after 4–24 h of aging, with values greater by ~1.7 than the peak microhardness of the Al–0.06 Sc alloy, but a microhardness value comparable with an Al–0.08 Sc alloy. The peak value is maintained for 96 h of aging, beyond which it decreases steadily, providing a first indication of the presence of over-aging and the onset of the growth and coarsening stage.

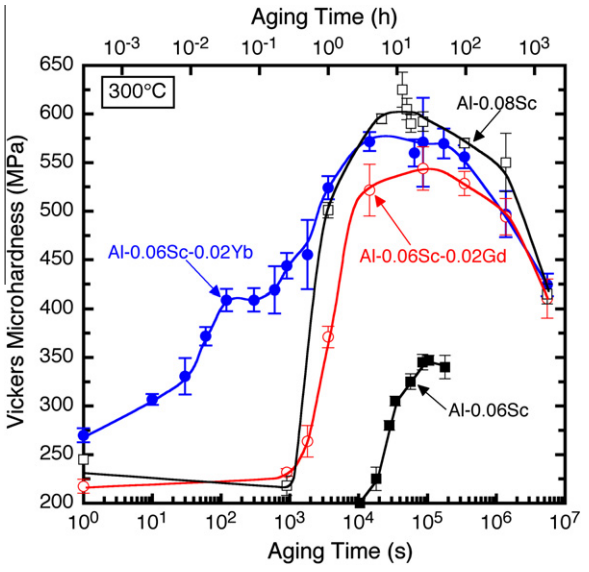

Fig. 1. Vickers microhardness of Al–0.06 Sc–0.02 Yb and Al–0.06 Sc–0.02 Gd vs aging time at 300 °C, compared with binary Al–0.06 Sc (reproduced from Refs. [10,12]) and Al–0.08 Sc alloys (reproduced from Ref. [53]).

Al–Sc–Yb exhibits a shorter incubation time than do Al–0.06 Sc, Al–0.12 Sc and Al–Sc–X alloys with similar volume fractions, ϕ, where X is Mg, Zr or Ti [10,31,54,65]. Whereas in these alloys the incubation times range from 0.25 to 2 h, Al–Sc–Yb exhibits an increased microhardness over the other aged Al alloys and pure Al upon quenching from the homogenization temperature (with no aging): 270 MPa compared with ~200 MPa for Al–0.06 Sc and Al–0.06 Sc–0.005 Zr alloys [65]. Upon subsequent aging, the microhardness increases rapidly: after 120 s at 300 °C it has increased over the homogenized value by 140 MPa. Before the final peak microhardness is achieved, there is an initial rapid increase in microhardness, followed by a plateau after 120 s, which is followed by a second rapid increase in microhardness. This is due to the disparate precipitation kinetics of Yb and Sc. The nucleation and growth (early aging times) in Al–Sc–Yb are similar to those for an Al–0.06Sc–0.005Yb alloy [54]. Initially, Yb-rich precipitates form and, subsequently, Sc reaches the precipitates and forms a shell enveloping the Yb-rich core.

3.2. Precipitate volume fraction, average radius and number density

For both Al–Sc–RE alloys, the $Al_3(Sc_{1-x}RE_x)$ precipitates are spheroidal and coherent with the matrix up to 1536 h, as indicated in Fig. 2 by the presence of Ashby–Brown or so-called "coffee-bean" strain-field contrast. The average precipitate radius $\langle R \rangle$ is <6 nm for both peak-aged and over-aged conditions in both alloys (Fig. 3). For Al–Sc–Yb, $\langle R \rangle$ increases from 2.9 ± 0.5 nm after 24 h (peak-aging) to 5.5 ± 1.2 nm after 1536 h at 300 °C (over-aging), as determined by LEAP tomography.

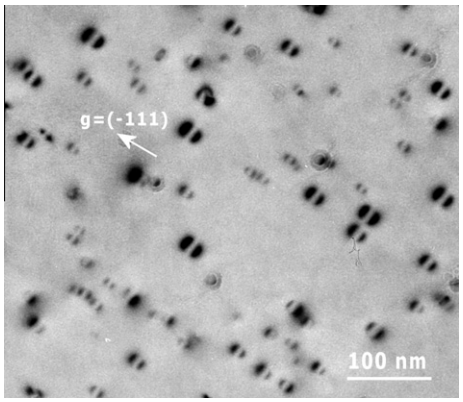

Fig. 2. Two-beam bright-field TEM image of Al–Sc–Yb aged for 1536 h (64 days) at 300 °C with the α′-precipitates exhibiting Ashby–Brown strain-field contrast, which is typical of coherent $Al_3(Sc_{1-x}Yb_x)$ α′-precipitates: [1 1 0] orientation.

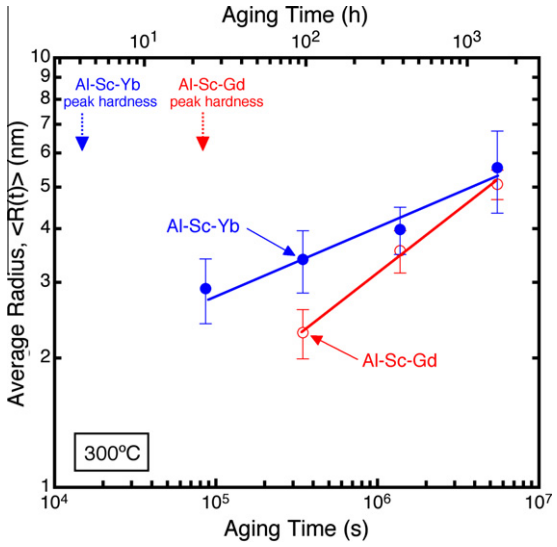

Fig. 3. Average α′-precipitate radius $\langle R(t)\rangle$ vs aging time at 300 °C for Al–Sc–Yb and Al–Sc–Gd. The slopes of the curves represent the temporal exponents. Only aging times past the peak microhardness are included.

For Al–Sc–Gd, $\langle R\rangle$ increases from 2.4 ± 0.3 nm to 5.1 ± 0.4 nm between 24 and 1536 h (Table 1). At a given aging time, Al–Sc–Gd has a smaller $\langle R\rangle$ value than does Al–Sc–Yb.

The precipitate number densities, N_v, were determined using LEAP tomographic data by counting the individual precipitates in the three-dimensional (3-D) reconstructions from two to three different samples. As demonstrated in Fig. 4 and Table 1, N_v achieves a maximum value of $(5.25 \pm 0.55) \times 10^{22}$ m^{-3} at 24 h for Al–Sc–Yb. The value of N_v at peak microhardness for Al–Sc–Gd is $(4.1 \pm 0.44) \times 10^{22}$ m^{-3} at 96 h. Both Al–Sc–RE alloys have higher N_v values than do Al–0.06Sc and Al–0.12Sc alloys with similar volume fractions: $\phi = 0.24\%$ and 0.49%, respectively [12]. Fig. 4 demonstrates that at 24 h for Al–Sc–Yb and 96 h for Al–Sc–Gd, N_v begins to decrease.

Table 1
Average α′-precipitate radii $\langle R\rangle$ and number densities N_v of Al–0.06 Sc–0.02 Yb and Al–0.06 Sc–0.02 Gd as a function of aging time t at 300 °C.

Alloy	t (h)	$\langle R\rangle$ (nm)	N_v (m^{-3})
Al–Sc–Yb	6	2.4 ± 0.4	$(4.7 \pm 0.5) \times 10^{22}$
	24	2.9 ± 0.5	$(5.3 \pm 0.6) \times 10^{22}$
	96	3.4 ± 0.6	$(2.1 \pm 0.2) \times 10^{22}$
	384	4.0 ± 0.5	$(7.5 \pm 1.4) \times 10^{21}$
	1536	5.5 ± 1.2	$(1.1 \pm 0.6) \times 10^{21}$
Al–Sc–Gd	24	2.4 ± 0.3	$(3.8 \pm 1.3) \times 10^{22}$
	96	2.3 ± 0.3	$(4.1 \pm 0.4) \times 10^{22}$
	384	3.6 ± 0.4	$(2.1 \pm 0.4) \times 10^{22}$
	1536	5.1 ± 0.4	$(5.7 \pm 2.1) \times 10^{21}$

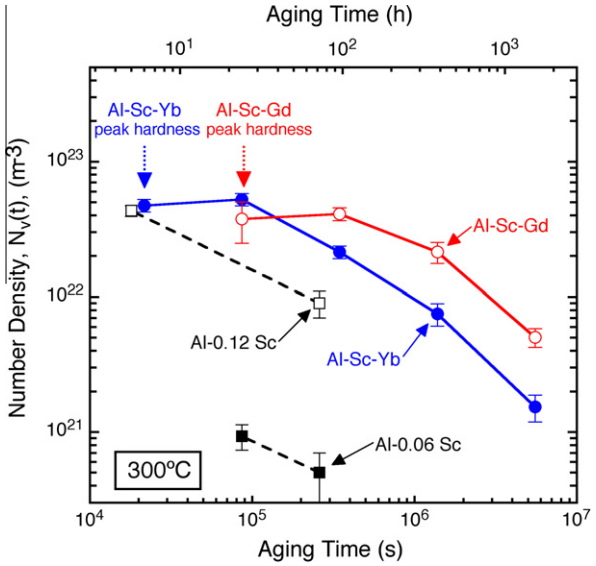

Fig. 4. Number density of α′-precipitates $N_v(t)$ vs aging time at 300 °C for Al–Sc–Yb and Al–Sc–Gd, compared with data from Al–0.06Sc and Al–0.12Sc alloys [12].

The volume fraction values are $\phi = 0.33 \pm 0.01\%$ for Al–Sc–Yb and $\phi = 0.28 \pm 0.01\%$ for Al–Sc–Gd, as determined for the longest aging time. These values were calculated from the fraction of solute atoms remaining in the matrix as determined by LEAP tomography. This fraction was then subtracted from the volume fraction calculated using the exact composition of the alloy to obtain the ϕ values for the precipitates. Fig. 5 demonstrates that the value of ϕ (t) is slowly increasing between 24 and 1536 h for both alloys, although the change (0.02% for Al–Sc–Yb and 0.005% for Al–Sc–Gd) is within experimental error, which indicates that growth of the precipitates is nearly complete, and ϕ is close to its equilibrium value ϕ_{eq}. The slowly changing values of ϕ indicate that the systems are most likely in a quasi-stationary state and in the growth and coarsening regime rather than pure coarsening. There is a 15% smaller value of ϕ in Al–Sc–Gd compared with Al–Sc–Yb, owing to a smaller Gd concentration in the precipitates compared with Yb in Al–Sc–Yb.

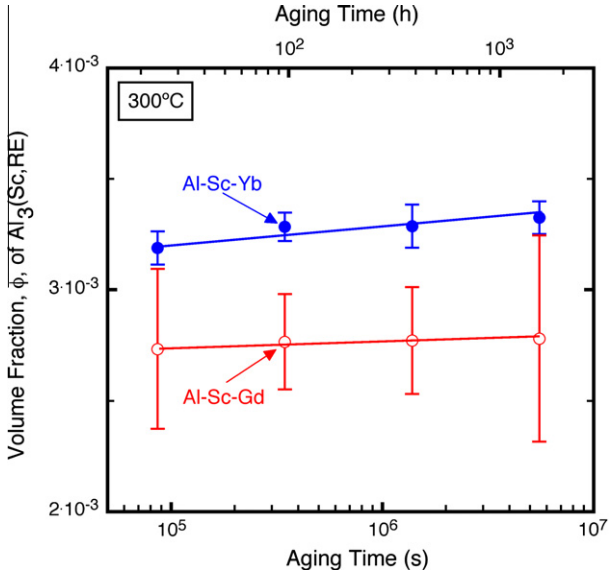

Fig. 5. Volume fraction ϕ of $Al_3(Sc,RE)$ α'-precipitates vs aging time at 300 °C for Al–Sc–Yb and Al–Sc–Gd alloys.

3.3. Compositional evolution

3.3.1. Al–Sc–Yb

The concentrations of Sc and RE in the precipitates were measured by LEAP tomography. Initially, in Al–Sc–Yb, the Yb/Sc atomic concentration ratio is large in the precipitates (Fig. 6), indicating that Yb precipitates faster than Sc does [54], thereby initially forming $Al_3(Yb_{1-x}Sc_x)$ precipitates. Fig. 7a indicates larger concentrations of Yb in the precipitates than Sc after 15 min of aging, especially near the center of the precipitates. With increasing aging time, the concentration of Sc in the precipitates increases steadily (Fig. 6), until it is greater than that of Yb after 6 h, resulting in precipitates with $Al_3(Sc_{1-x}Yb_x)$ compositions. The Yb/Sc ratio in the $Al_3(Sc_{1-x}Yb_x)$ achieves a constant value of 0.25 ± 0.01 after 96 h of aging, somewhat below the overall alloy ratio of 0.41. The concentrations of Sc and RE in the α-Al matrix were also measured at longer aging times by LEAP tomography (Fig. 8a). In the matrix, the Yb and Sc concentrations are decreasing with increasing aging time even at the longest aging time (Fig. 8a), which is consistent with an increasing volume fraction.

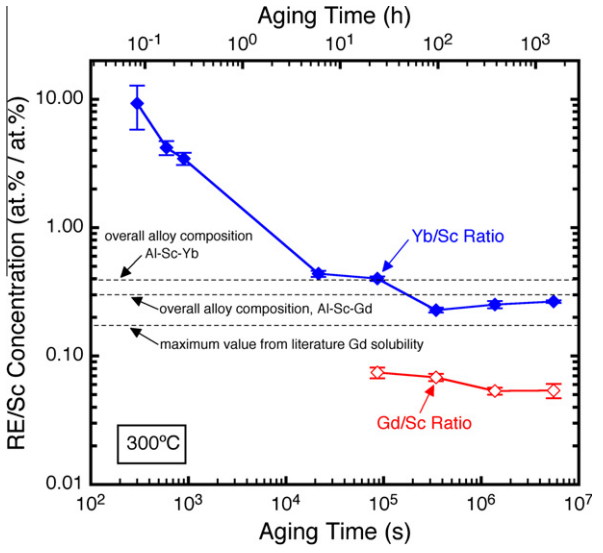

Fig. 6. RE/Sc atomic concentration ratio in the α'-precipitates vs aging time at 300 °C for Al–Sc–Yb and Al–Sc–Gd.

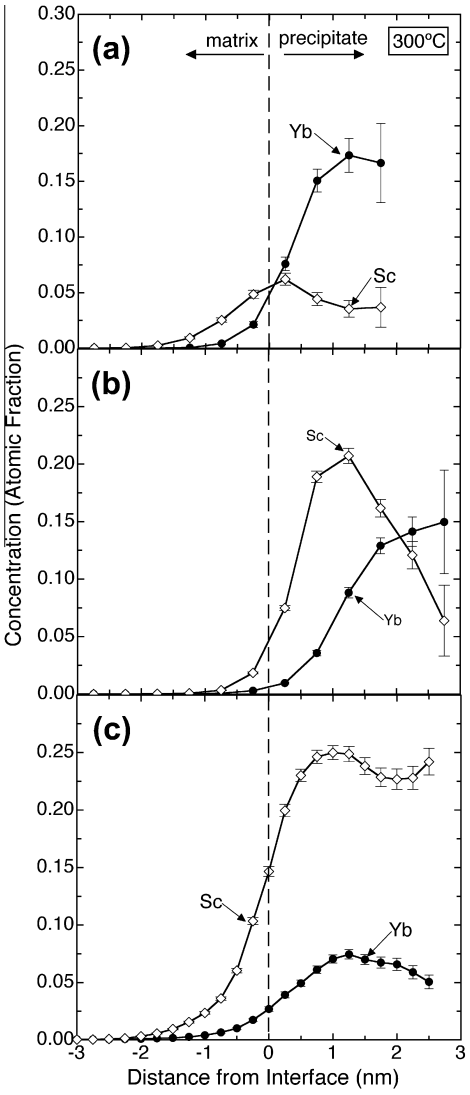

Fig. 7. Proximity histograms of Al–Sc–Yb exhibiting the average concentrations of Yb and Sc as a function of radial distance from the heterophase interface ($x = 0$) for different aging times at 300 °C: (a) 15 min; (b) 24 h; (c) 1536 h.

The distribution of elements within the precipitates in Al–Sc–Yb after 24 h of aging is displayed in Figs. 7, 9 and 10. In Fig. 9, a Sc-rich spherical shell enveloping a Yb-rich core is observed from a slice through a 3-D LEAP tomographic reconstruction. In Fig. 10, a 3-D reconstruction is displayed, which exhibits 8 at.% Yb isoconcentration surfaces delineating the precipitate cores that are enveloping Sc-rich shells. The core/shell structure is also

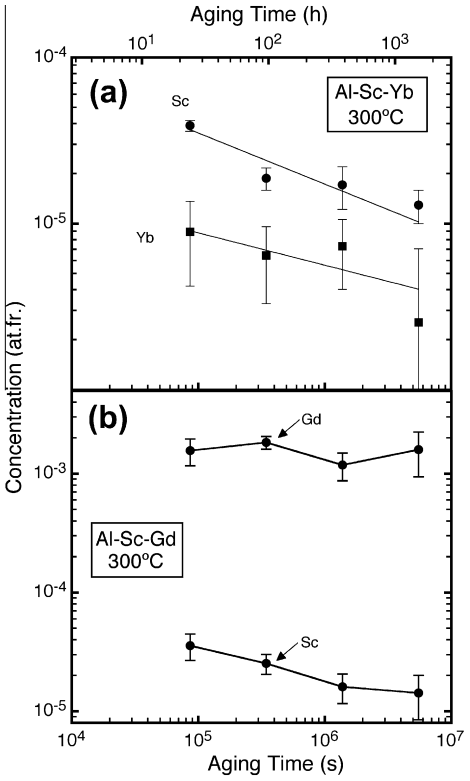

Fig. 8. (a) Concentrations of Yb and Sc in the α-Al matrix vs aging time at 300 °C in Al–Sc–Yb. (b) Concentrations of Gd and Sc in the α-Al matrix vs aging time at 300 °C for Al–Sc–Gd.

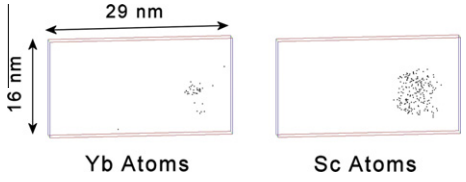

Fig. 9. LEAP tomographic reconstructions of Al–Sc–Yb showing the core/shell atomic structure of an $Al_3(Sc_{1-x}Yb_x)$ α′-precipitate after 24 h of aging at 300 °C: 2-nm-thick slice.

observed in the proxigram after aging for 24 h (Fig. 7b), with a pronounced segregation of Sc at the α-Al/$Al_3(Sc_{1-x}Yb_x)$ interface. After aging for 1536 h (64 days), the Yb-rich core is less pronounced, as the Sc concentration now exceeds the Yb concentration everywhere within the precipitates (Fig. 7c). Note that the Sc + Yb concentrations sum to >25%. This is most probably due to differences in field-evaporation behavior between the elements. This appears to become more pronounced as the precipitate size grows [66–68].

At 1536 h, some segregation of Sc at the heterophase interfaces is still observed: Fig. 11 indicates positive values of the relative Gibbsian interfacial excess of Sc at the α-Al/$Al_3(Sc_{1-x}Yb_x)$ interface, which is given by [69,70]:

$$\Gamma_{Sc}^{Al,RE} = \Gamma_{Sc} - \Gamma_{RE}\left(\frac{C_{Al}^{\alpha}C_{Sc}^{\alpha'} - C_{Al}^{\alpha'}C_{Sc}^{\alpha}}{C_{Al}^{\alpha}C_{RE}^{\alpha'} - C_{Al}^{\alpha'}C_{RE}^{\alpha}}\right) - \Gamma_{Al}\left(\frac{C_{Sc}^{\alpha}C_{RE}^{\alpha'} - C_{Sc}^{\alpha'}C_{RE}^{\alpha}}{C_{Al}^{\alpha}C_{RE}^{\alpha'} - C_{Al}^{\alpha'}C_{RE}^{\alpha}}\right) \quad (1)$$

where α is the matrix phase (α-Al), α′ is the precipitate-phase, C_j^i is the concentration of the jth element in the ith phase, and $\Gamma_j^{Al,RE}$ is the relative Gibbsian interfacial excess of element j with respect to Al and RE. Fig. 11 indicates decreasing values of $\Gamma_{Sc}^{Al,Yb}$ up to 1536 h of aging, consistent with the less pronounced core/shell structure at longer aging times.

3.3.2. Al–Sc–Gd

In Al–Sc–Gd, precipitation occurs less rapidly than in Al–Sc–Yb, which does not increase above the homogenized microhardness value until after 15 min of aging at 300 °C. For the Al–Sc–Gd alloy (Fig. 6), the Gd/Sc ratio in the precipitates is <1, since there is less Gd than Sc in the precipitates. After 24 h, the concentration of Gd in the precipitates is 2.7 ± 0.2 at.%. At aging times of 96 h and longer, the Gd concentration decreases and then remains approximately constant at 2.0 ± 0.4 at.%. Furthermore, the onset of coarsening of the precipitates in Al–Sc–Gd

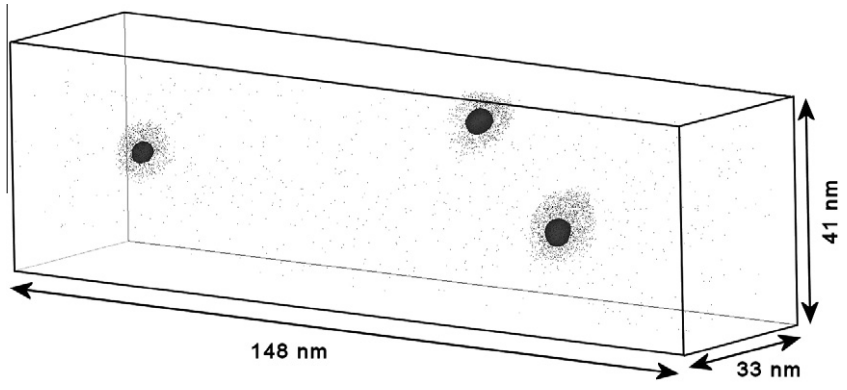

Fig. 10. Three-dimensional LEAP tomographic reconstruction exhibiting three $Al_3(Sc_{1-x}Yb_x)$ α′-precipitates in an Al–Sc–Yb alloy for a 24 h aging time at 300 °C. The 8 at.% Yb isoconcentration surface within the α′-precipitates delineates the Yb core, with the Sc atoms engulfing the Yb core. Total volume of the rectangular parallelepiped is 200,244 nm^3. The Al atoms are omitted for clarity.

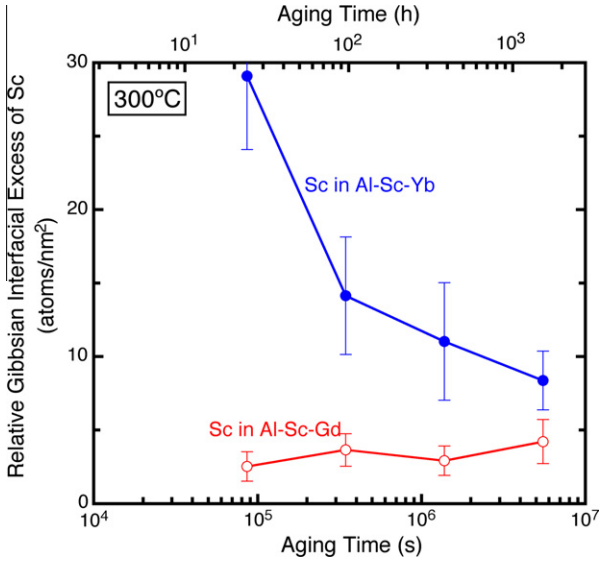

Fig. 11. Relative Gibbsian interfacial excess of Sc with respect to Yb or Gd in Al–Sc–Yb at the α-Al/$Al_3(Sc_{1-x}Yb_x)$ interface and in Al–Sc–Gd at the α-Al/$Al_3(Sc_{1-x}Gd_x)$ interface vs aging time at 300 °C.

occurs after 96 h, since the N_v value remains constant between 24 and 96 h (Fig. 4). In the α-Al matrix in Al–Sc–Gd (Fig. 8b), the Sc matrix concentration decreases up to 1536 h of aging, while the Gd matrix concentration is constant between 24 and 1536 h of aging. Heterophase interfacial segregation of Sc is observed for all aging times, with the Gd tending toward the center of the precipitates. The relative Gibbsian interfacial excess of Sc with respect to Al and Gd, $\Gamma_{Sc}^{Al,Gd}$, at the α-Al/$Al_3(Sc_{1-x}Gd_x)$ interface (Eq. (1)), increases slightly during the growth and coarsening regime (Fig. 11).

3.4. Creep

Figs. 12 and 13 demonstrate that the Al–Sc–RE alloys exhibit creep behavior at 300 °C characterized by a high

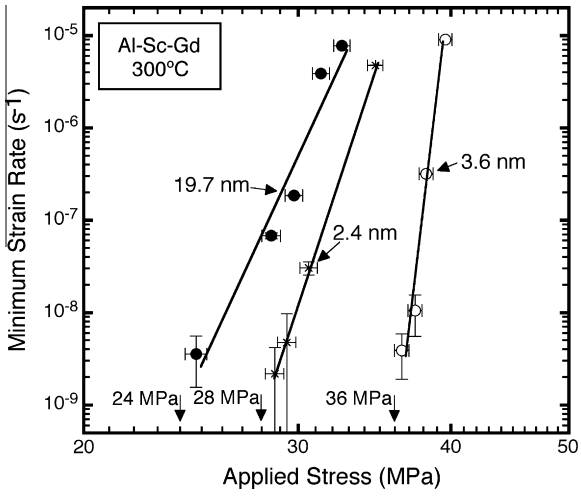

Fig. 12. Minimum strain rate vs applied stress for Al–Sc–Gd alloy at 300 °C. Threshold stresses are marked on the stress axis.

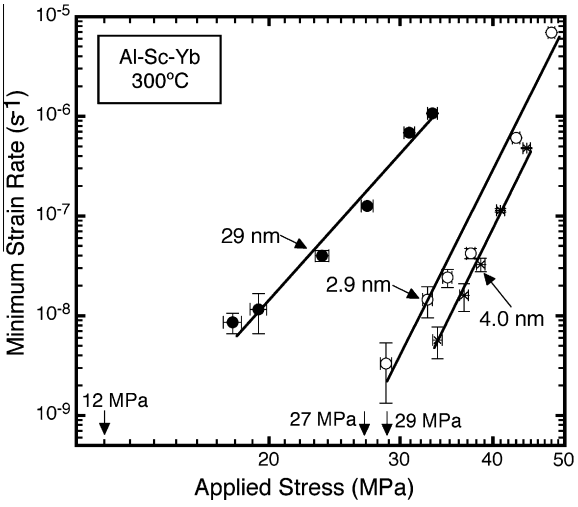

Fig. 13. Minimum strain rate vs applied stress for Al–Sc–Yb alloy at 300 °C. Threshold stresses are marked on the stress axis.

apparent stress exponents of $n_{ap} = 29$–37 (slope in the double logarithmic plots), which is indicative of the presence of a threshold stress σ_{th}, below which the creep rate $\dot{\varepsilon}$ cannot be experimentally measured [71]. The power-law creep equation that includes a threshold stress is

$$\dot{\varepsilon} = A(\sigma - \sigma_{th})^n \exp\left(-\frac{Q}{R_g T}\right) \quad (2)$$

where A is the Dorn constant, σ is the applied stress, $Q = 142$ kJ mol^{-1} is the activation energy for creep in pure Al [72], $n = 4.4$ is the stress exponent of pure Al [72], and R_g is the ideal gas constant. By plotting $\dot{\varepsilon}^{1/n}$ vs σ [73], threshold stresses are calculated, and their values are displayed on the abscissa axes of Figs. 12 and 13.

4. Discussion

4.1. Temporal evolution of precipitate composition

The LEAP tomographic results for Al–Sc–Yb demonstrate that the initial $Al_3(Yb_{1-x}Sc_x)$ precipitates are richer in Yb than Sc. After 5 min of aging, the Yb/Sc concentration ratio is 9.3 (Fig. 6). The rapid precipitation of Yb is a kinetic effect due to the larger diffusivity of Yb in the alloy D_{Yb}, at least in the initial stages. The diffusivity of Yb in a binary Al–0.03Yb is greater than that of Sc in Al [42]. For Al–Sc–RE with RE = Tb, Ho, Tm or Lu [56], a similar rapid precipitation with an initial rise in microhardness due to the precipitation of a RE element was observed.

Sc diffuses to the precipitates at a slower rate because it has a smaller diffusivity, D_{Sc}, in Al–Sc–Yb than does Yb. As the Sc diffuses to the precipitates, it first forms a spheroidal shell enveloping the $Al_3(Yb_{1-x}Sc_x)$ precipitates, as demonstrated by the 3-D LEAP tomographic reconstructions (Figs. 9 and 10). With increasing aging time at 300 °C, the Yb-rich core and Sc-rich shell inter-diffuse (Fig. 7), confirming that Yb and Sc can substitute for

one another in the $Al_3(Sc,Yb)$ precipitates and also indicating that Yb replaces some of the more expensive Sc, while retaining a constant value of ϕ. The maximum solubility of Yb in α-Al is 248 ± 7 at.ppm Yb based on LEAP tomographic measurements on Al–0.06Yb, which was aged at the eutectic temperature of 625 °C for 72 h [53]. This limits the amount of Yb that can replace Sc.

The Yb/Sc atomic concentration ratio in the precipitates achieves a value of 0.23 after 96 h of aging and remains relatively constant at longer times (Fig. 6). Nevertheless, the value of the relative heterophase interfacial excess of Sc continues to decrease with increasing aging time up to 64 days, indicating that the system has not achieved a stationary state (Fig. 11). Since the distribution of the elements within the precipitates evolves continuously up to the longest aging time, the coarsening constants associated with the supersaturation of each of the elements in the precipitates could not be measured, because the average composition of the precipitates could not be accurately determined. Furthermore, since the interdiffusion of the Yb and Sc core/shell layers is slow because of the highly correlated diffusion in the ordered $Al_3(Sc,Yb)$ precipitates, it is estimated from the evolution of the precipitate concentrations that the Sc diffusivity within $Al_3(Yb_{1-x}Sc_x)$ is $\sim 3 \times 10^{-26}\ m^2\ s^{-1}$ at 300 °C. This is six orders of magnitude smaller than the Sc diffusivity in the α-Al matrix [27]. A recent study using LKMC simulations found that Zr segregation at the α-Al/$Al_3(Sc_{1-x}Zr_x)$ interface is kinetically limited [28]. By setting the diffusivity of both elements equal in the LKMC simulation, such that the elements diffuse to the precipitates at the same rate, a uniform distribution of elements is observed in the precipitates.

In the Al–Gd system, the precipitates have the DO_{19} structure [74]. For the Al–Sc–Gd system, the $L1_2$ $Al_3(Sc_{1-x}Gd_x)$ precipitates form with <10% of the Gd atoms contained in the precipitates, as determined by LEAP tomography. The concentration of Gd in the precipitates is smaller than the Yb concentration in the $Al_3(Sc_{1-x}Yb_x)$ precipitates in Al–Sc–Yb for a given aging treatment. After 24 h of aging, the Gd concentration in the precipitates is 2.1 at.%, while the Yb concentration in the precipitates is 7.4 at.% in Al–Sc–Yb. The Gd concentration remains approximately constant at 2 at.% to the longest aging time (Fig. 6), which is less than the maximum solubility of Gd in Al_3Sc at the eutectic temperature, 3.75 at.% Gd [35]. This makes Gd a less interesting candidate for use in Al–Sc–X alloys for replacing Sc. This small Gd concentration may also be the reason for the absence of an increase in peak microhardness in Al–Sc–Gd with 200 at.ppm Gd compared with an Al–Sc–Gd alloy with 50 at.ppm of Gd [54]. Both alloys have a similar concentration of Gd in the precipitates, and thus the additional Gd in Al–Sc–Gd does not increase the value of ϕ.

Gd partitions to the center of the precipitates, as observed in Al–0.06Sc–0.005Gd [54]. The relative Gibbsian heterophase interfacial excess of Sc at the α-Al/$Al_3(Sc_{1-x}Gd_x)$ interface increases slightly in the range of aging times from 24 to 1536 h, indicating that the Gd is diffusing to the center of the precipitates. A quasi-stationary state of elements within the precipitates is not achieved and hence the coarsening constants associated with the supersaturation in the α′-precipitates are not calculated. When compared with Al–Sc–Yb, the relative Gibbsian heterophase interfacial excess of Sc at the α-Al/$Al_3(Sc_{1-x}Gd_x)$ interface in Al–0.06Sc–0.005Gd is smaller (Fig. 11), perhaps because the Gd atoms appear to precipitate simultaneously with the Sc atoms. In contrast, in Al–Sc–Yb, the Yb precipitates long before the Sc does, hence eliminating the need for Yb to diffuse to the center of the precipitates.

4.2. Nanostructure and volume fraction

One reason for the larger peak microhardness values in Al–Sc–Yb and Al–Sc–Gd (Fig. 1), compared with Al–0.06Sc, is the larger volume fraction of precipitates in the ternary alloys ($\phi = 0.33$ and 0.28%, respectively), compared with Al–0.06Sc (0.24% [1]). In addition, compared with the Al–0.06Sc alloy [1], the Al–Sc–Yb and Al–Sc–Gd alloys have increased N_v values by more than an order of magnitude [12]. The Al–0.12Sc alloy does, however, have a larger microhardness with values of N_v equal to or lower than the Al–Sc–Yb and Al–Sc–Gd alloys, as a result of its larger volume fraction [1]. Both the increased values of N_v and ϕ as well as the smaller $\langle R \rangle$ value contribute to a larger value of the Orowan stress, which can be estimated to be 1/3 of the microhardness increment [75]. For an Al–0.08Sc alloy with the same solute content as the ternary alloys, the microhardness is about the same as for Al–Sc–Yb and slightly greater than for Al–Sc–Gd [53], indicating that Yb and Gd effectively replace the more expensive Sc.

Binary alloys with similar values of ϕ ($\phi = 0.24\%$ for Al–0.06Sc and $\phi = 0.49\%$ for Al–0.12Sc) have smaller or equal N_v values [1,12] with maximum measured N_v values of 9.3×10^{20} and $4.3 \times 10^{22}\ m^{-3}$, respectively (Fig. 4). Thus, small additions of RE increase N_v significantly. A similar increase in the microhardness of the alloys and N_v values of precipitates was observed for Al–Sc–RE alloys with $0.005 \pm 0.003\%$ RE, which have $\phi = 0.22\%$ and 0.25% for the Yb and Gd additions, respectively [54]. It is apparent that microalloying with RE additions alters significantly the precipitation kinetics of Al–Sc alloys.

The quasi-stationary-state nucleation current for precipitates with radii greater than the critical radius R^* is calculated for the Al–Sc–Yb alloy. Sub-critical precipitates (that is, embryos) exist below a critical radius R^*, while for $R > R^*$, precipitates (nuclei) are present. The nucleation rate is estimated from the 30 s and 120 s aging times to be $1.91 \times 10^{20}\ m^{-3}\ s^{-1}$. Hyland [4] found that, for an Al–0.11Sc alloy, the quasi-stationary-state nucleation current is $9 \times 10^{18}\ m^{-3}\ s^{-1}$ at 288 °C and $1.01 \times 10^{19}\ m^{-3}\ s^{-1}$ at 343 °C, respectively, which are smaller than the quasi-stationary-state nucleation current for the Al–Sc–Yb alloy.

The larger nucleation current in the ternary alloys could be due to the following: (i) clusters of RE elements in the as-quenched state serve as effective heterogeneous nucleation sites for precipitates; (ii) the chemical driving force is greater than in the Al–Sc alloys; or (iii) the interfacial Gibbs free energy σ between the $L1_2$ precipitate phase and α-matrix phase is smaller in Al–Sc–Yb than in Al–Sc alloys.

4.3. Precipitate coarsening

The Lifshitz–Slyozov–Wagner (LSW) diffusion-limited coarsening model for binary alloys [76–78] has been extended to concentrated multicomponent alloys by Umantsev and Olson [79], and analyzed in detail for ternary alloys, including capillary effects, by Kuehmann and Voorhees (KV) [80]. The time exponent for the evolution of $\langle R\rangle$ of the ternary alloys is predicted to be 1/3, the same as for the binary alloys, albeit with a different rate constant, K_{KV}, from the LSW model. Similarly, the coarsening constants for non-ideal and non-dilute alloys can be significantly different from those of dilute alloys, although the time exponents are the same [81].

The following equations from the KV model for coarsening of a ternary alloy [80] are used to analyze the data for the longer aging times in the Al–Sc–Yb and Al–Sc–Gd alloys. These equations assume that quasi-stationary coarsening is occurring:

$$\langle R(t)\rangle^3 - \langle R(t_o)\rangle^3 = K_{KV}(t - t_o) \tag{3}$$

$$N_v(t)^{-1} - N_v(t_o)^{-1} = 4.74\frac{K_{KV}}{\phi_{eq}}(t - t_o) \tag{4}$$

$$\Delta C_i^{\alpha}(t) = \langle C_i^{\alpha,ff}(t)\rangle - C_i^{\alpha,eq}(\infty) = \kappa_{i,KV}^{\alpha}(t)^{-1/3} \tag{5}$$

where K_{KV} and $\kappa_{i,KV}^{\alpha}$ are the coarsening rate constants for $\langle R(t)\rangle$ and $\Delta C_i^{\alpha}(t)$, respectively; $\langle R(t_o)\rangle$ is the average precipitate radius at the onset of quasi-stationary coarsening at time t_o and $N_v(t_o)$ is the precipitate number density at the onset of quasi-stationary coarsening at time t_o. The quantity $\Delta C_i^{\alpha}(t)$ is the supersaturation and is the difference between the concentration in the far-field (*ff*) α-matrix, $\langle C_i^{\alpha,ff}(t)\rangle$ and the equilibrium α-matrix solute-solubility $C_i^{\alpha,eq}(\infty)$. The quantity ϕ_{eq} represents the equilibrium volume fraction of the precipitating phase. The quantity $C_i^{\alpha,eq}(\infty)$ needs to be determined experimentally, as it is not available for Al–Sc–Yb at 573 K.

After 24 h of aging for Al–Sc–Yb and 96 h of aging for Al–Sc–Gd, N_v begins to decrease, while $\langle R(t)\rangle$ is concomitantly increasing. This, combined with the negligible increase in volume fraction beyond these aging times (Fig. 5), indicates that the system is near to quasi-stationary state coarsening ($\frac{\partial C_i}{\partial t} \approx 0$). This concurrent growth and coarsening is also observed in the Ni–Al–Cr system [82–86]. Furthermore, Fig. 14 displays the product of N_v and t vs aging time t, which should be a constant if the system is in a stationary state. For both Al–Sc–RE alloys, this

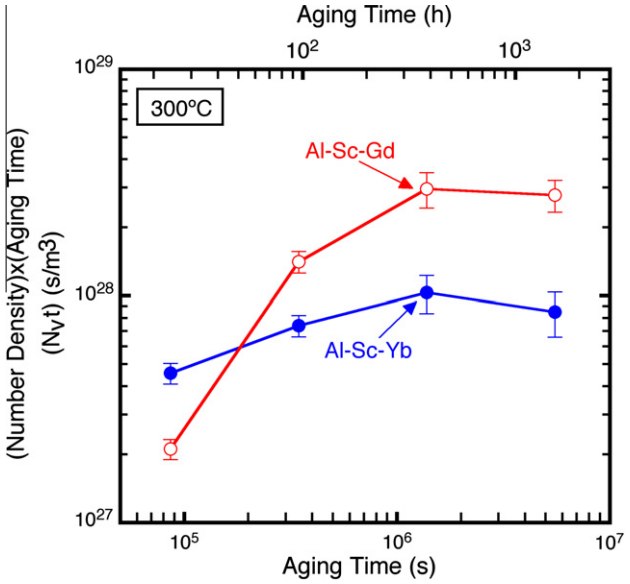

Fig. 14. Product of number density $N_v(t)$ and aging time vs aging time at 300 °C for the Al–Sc–Yb and Al–Sc–Gd alloys.

product is increasing with aging time up to 16 days (384 h). Thus, neither alloy has achieved a stationary state, since the distribution of the elements within the precipitates is changing up to 1536 h (Section 4.3), and there is still a slight increase in ϕ (Fig. 5). Therefore, the two alloys are most likely in a quasi-stationary state and not a stationary state.

4.3.1. Evolution of average precipitate radius

The time exponent for the temporal evolution of $\langle R(t)\rangle$ (Eq. (3)), derived using a multiple linear regression-analysis, is 0.18 ± 0.03 for Al–Sc–Yb and 0.22 ± 0.01 for Al–Sc–Gd. These alloys are thus coarsening more slowly than predicted by the KV coarsening model, while prior studies on Al–Sc binary alloys exhibit a $t^{1/3}$ dependence [5,11–13,16–18]. The Al–Sc–Zr [21] and Al–Sc–Ti [31] alloys also have time exponents <1/3, in the range 0.05–0.1, indicating that Yb and Gd are not as effective at slowing the coarsening as are Zr or Ti. A practical rule of thumb is that $\langle R(t)\rangle$ needs to increase by a factor of 10 to determine a meaningful value of its temporal exponent, which is not the case for either ternary alloy. The same rule applies for the two other temporal exponents. The coarsening constant K_{KV} (Eq. (3)) was also determined from the experimental data using a multiple linear regression analysis (also taking into account the values of t_o and $\langle R(t)\rangle$). For Al–Sc–Yb, K_{KV} is equal to $(2.87 \pm 0.3) \times 10^{-32}\ m^3\ s^{-1}$ and for Al–Sc–Gd K_{KV} it is $(2.19 \pm 0.12) \times 10^{-32}\ m^3\ s^{-1}$.

4.3.2. Temporal evolution of the precipitate number density

Fig. 4 demonstrates that the onset of coarsening occurs at a later time for Al–Sc–Gd than for Al–Sc–Yb, as determined by the first decrease in N_v. After the nucleation and growth stage, this alloy exhibits both growth and

coarsening. The experimental time exponents for the evolution of N_v (Eq. (4)), calculated using a multiple regression analysis, are -0.84 ± 0.05 for Al–Sc–Yb and -0.76 ± 0.06 for Al–Sc–Gd. They thus differ from the predicted KV model value of -1 (Eq. (4)), which implies that a stationary-coarsening state has not been achieved. While it is assumed, based on the smaller diffusivities of the other light RE elements (La to Sm), that Gd diffuses less rapidly than Sc, it does not appear that, once coarsening commences, it has a significant effect on decelerating the coarsening rate. These temporal exponents demonstrate that Yb and Gd are not as effective at decelerating the coarsening kinetics as Zr [21], where temporal exponents for similar aging treatments were found to be close to zero and in some cases positive, indicating that coarsening has not commenced. The later onset of coarsening in Al–Sc–Gd may be due to disparate precipitation mechanisms in the two alloys.

4.3.3. Temporal evolution of matrix supersaturations

The equilibrium solid-solubilities of Yb and Sc in the α-Al matrix of Al–Sc–Yb were calculated for infinite time at 300 °C (Eq. (5)), using a multiple linear regression analysis (Fig. 8a). For Al–Sc–Yb, the equilibrium solubilities in the α-Al matrix are found to be 2.5 ± 1 at.ppm for Yb and 2.7 ± 1 at.ppm for Sc at 300 °C. The equilibrium concentration of Al in the α-matrix is determined in a similar manner to that of Yb and Sc, and is found to be 99.9995 ± 0.0098 at.%. This validates the fitting procedure, since the concentrations of the three elements sum to 100%.

For Al–Sc–Yb, the rate constant for the supersaturation of Yb in the α-Al matrix in Eq. (5), $\kappa_{Yb}^{\alpha,KV}$, is $(3.0 \pm 3.4) \times 10^{-4}$ at.fr. s^{-3}, while for the Sc supersaturation the value for $\kappa_{Sc}^{\alpha,KV}$ is $(1.5 \pm 0.2) \times 10^{-3}$ at.fr. s^{-3}. The rate constant for the Al supersaturation in the α-Al matrix, $\kappa_{Al}^{\alpha,KV}$, is $(-1.8 \pm 2.8) \times 10^{-3}$ at.fr. s^{-3}. The rate constants sum to zero, which validates the fitting procedure employed for the rate constants.

For Al–Sc–Yb, the measured temporal exponent for Yb is -0.10 ± 0.03 and for Sc it is -0.23 ± 0.04. The values of the temporal exponents are less than the $-1/3$ value predicted by the KV coarsening model [80], indicating that the coarsening is occurring at a slower rate than predicted. When compared with the Al–Sc–Zr system, the temporal exponents for the supersaturation are similar [9]; the Sc and Zr supersaturations have temporal exponents of -0.33 and -0.11, respectively: the latter is because of the small diffusivity of Zr in Al. In binary Al–Sc alloys, there have been several studies which monitored the supersaturation of Sc using electrical resistivity measurements; Al–0.15% Sc in the temperature range 533–733 K [2] and Al–0.17% Sc in the temperature range 673–723 K [16], and it was found that ΔC_{Sc}^{α} decays with a $t^{-1/3}$ dependence. This indicates that, similarly to the $\langle R(t) \rangle$ evolution, the coarsening rate diminishes compared with binary Al–Sc alloys when Yb is added.

Applying the above procedures to Al–Sc–Gd, the equilibrium solubility of Sc is found to be 5.8 ± 2 at.ppm Sc (Fig. 8b). $\kappa_{Sc}^{\alpha,KV}$ for Al–Sc–Gd is $(1.4 \pm 0.6) \times 10^{-3}$ at.fr. s^{-3}, and the time exponent for ΔC_{Sc}^{α} is -0.32 ± 0.02, which is close to the KV model value [80]. The majority of the Gd (91% at $\sim 150 \pm 10$ at.ppm) remains in the α-matrix and is not dissolved in the precipitates at 1536 h. The quantity ΔC_{Gd}^{α} and the time exponent for the Gd supersaturation in the α-Al matrix were not calculated because a significant fraction of the Gd atoms remain in the α-matrix, and the change in its concentration in the α-matrix during coarsening is within the experimental measuring error.

The presence Gd or Yb has an effect on the Sc solubility in the α-Al matrix. The values of the Sc solubility in α-Al for both Al–Sc–RE alloys (10 at.ppm for Al–Sc–Yb and 5.81 at.ppm for Al–Sc–Gd) are smaller than that measured in an Al–2.2 Mg–0.12 Sc alloy (89 ± 30 at.ppm Sc) [87], and also smaller than measured in a binary Al–0.15 Sc alloy (50 at.ppm Sc) [2]. A recent study of an Al–0.09 Sc–0.047Zr alloy yielded an even higher solid-solubility of Sc, 120 ± 30 at.ppm, although the value from the calculated ternary phase diagram presented in this reference is only 7 at.ppm Sc [9].

4.3.4. Interfacial free energy and diffusivity of Yb in the matrix

The diffusivity and interfacial free energy for a binary alloy can be calculated from coarsening data using an approach developed by Ardell [88]. His approach has been applied to a binary Al–0.17 Sc alloy in the range 673–723 K [16]. The interfacial free energy has also been calculated for an Al–0.15 Sc alloy [2]. Ardell's approach has been extended to a ternary alloy [87], and also to a non-dilute ternary alloy [86].

The expression for diffusivity of Yb in this alloy at 300 °C, D_{Yb}, and the interfacial free energy $\sigma^{\alpha/\alpha'}$ are given by [87]

$$D_{Yb} = \frac{\Delta C_{Yb}(\Delta C_{Yb} G''_{YbYb} + \Delta C_{Sc} G''_{YbSc})}{\frac{4}{9}\frac{\kappa_{KV}}{\Delta C_{Yb} K_{KV}^{2/3}} \Delta C_{Yb}(\Delta C_{Yb} G''_{YbYb} + \Delta C_{Sc} G''_{YbSc}) + \Delta C_{Sc}(\Delta C_{Yb} G''_{YbSc} + \Delta C_{Sc} G''_{ScSc}) - \frac{\Delta C_{Sc}}{D_{Sc}}(\Delta C_{Yb} G''_{YbSc} + \Delta C_{Sc} G''_{ScSc})} \tag{6}$$

and

$$\sigma^{\alpha/\alpha'} = \frac{\kappa_{KV} K_{KV}^{1/3}(\Delta C_{Yb}(\Delta C_{Yb} G''_{YbYb} + \Delta C_{Sc} G''_{YbSc}) + \Delta C_{Sc}(\Delta C_{Yb} G''_{YbSc} + \Delta C_{Sc} G''_{ScSc}))}{2 V_m \Delta C_{Yb}} \tag{7}$$

where $G''_{i,j}$ are the second derivatives of the Gibbs free energy with respect to concentration (assuming a dilute ideal solid-solution in the essentially complete absence of a thermodynamic database for Al–Sc–RE alloys), ΔC_i is $(C_{\text{precipitate}} - C_{\text{matrix}})$ of element i, and V_m is the molar volume of the $Al_3(Sc,Yb)$ phase as calculated from lattice parameters of the $Al_3(Sc,Yb)$ phase ($V_m = 1.035 \times 10^{-5}$ m^3 mol^{-1}).

Eqs. (6) and (7) were used, employing the experimentally measured coarsening constants, to calculate D_{Yb} in the ternary alloy and $\sigma^{\alpha/\alpha'}$ between the α-Al matrix and α′-precipitate phases in the coarsening regime [87]. This method assumes that the system is in the coarsening regime. Although the coarsening time exponents vary somewhat from the predictions of the model, there is only a slight increase in ϕ (Fig. 5). Therefore, the two alloys are close to the coarsening regime, but most likely in a quasi-stationary state and not a stationary state. The calculated diffusivity of Yb in Al–Sc–Yb is $D_{Yb} = (5 \pm 4) \times 10^{-21}$ m^2 s^{-1} at 300 °C. It is known experimentally, however, that Yb precipitates out of the matrix before Sc [54,89]. The value of D_{Yb} calculated for earlier aging times (before the majority of the Sc forms precipitates) ranges from 10^{-19} to 10^{-18} m^2 s^{-1}, depending on the method used to calculate D_{Yb} [89] (Table 2). During the coarsening stage, a probable reason for the smaller value of D_{Yb} is that Yb may be kinetically trapped in the interior of the precipitates. It is well known that diffusion is more correlated in ordered structures than in the disordered matrix and hence occurs at a slower rate [90] than in the α-Al matrix.

The value of D_{Yb} calculated for the binary Al–Yb alloy, $(5.7 \pm 1.9) \times 10^{-17}$ m^2 s^{-1} [89], is faster than D_{Yb} measured for Al–Sc–Yb either during the early aging period or after 24 h of aging. In addition, beyond 24 h of aging, D_{Yb} is smaller than the value of D_{Sc} in binary Al–Sc alloys, which is 9×10^{-20} m^2 s^{-1} at 300 °C [27]. Furthermore, the presence of Sc decreases the value of D_{Yb}, implying that the off-diagonal terms of the diffusion tensor are most likely non-zero [91].

A value of D_{Sc} is also calculated using the same procedure as in Eqs. (6) and (7). The value $D_{Yb} = (5.7 \pm 1.9) \times 10^{17}$ m^2 s^{-1} [89], which is the value measured for the binary Al–Yb alloy, is put into the calculation. A value of $D_{Sc} = (4.9 \pm 3.1) \times 10^{-20}$ m^2 s^{-1} is measured. This is within an order of magnitude of the literature value for a binary Al–Sc alloy [12,27]. The Sc is contained mostly in the shell enveloping the precipitates and is hence not kinetically trapped within the intermetallic precipitate.

The interfacial free energy $\sigma^{\alpha/\alpha'}$ for Al–Sc–Yb at 300 °C is calculated to be 670 ± 150 mJ m^{-2}. This is significantly greater than the value calculated using a similar method for Al–Sc alloys, where a value of ~200 mJ m^{-2} was obtained at 300 °C [12,92]. For Al–2.2 Mg–0.12 Sc (at.%), $\sigma^{\alpha/\alpha'}$ is 158 ± 36 mJ m^{-2} [87], and 225 mJ m^{-2} for Al–1.1 Mg–0.16 Sc at 400 °C (at.%) [93]. For the Al–Yb binary alloy, the value for the Al/Al_3Yb interface was calculated to be 600 ± 300 mJ m^{-2} at 300 °C [42]. Recently, first-principles calculations of interfacial energies (0 K) of $Al/Al_3Gd(1\,0\,0)$ and $Al/Al_3Yb(1\,0\,0)$ interfaces were performed, using the Vienna ab initio Simulation Package [94]. The calculated values for these (1 0 0) interfaces are 339 mJ m^{-2} and 333 mJ m^{-2}, respectively, which are significantly less than the experimental values calculated employing the assumption of an ideal solid-solution. It is therefore highly likely that the assumption of an ideal solid-solution is too strong based on the above interfacial energies calculated at 0 K using first-principles calculations. Calculation of the temperature dependence of these interfacial energies taking into account the vibrational entropy contribution should decrease the 0 K values.

4.4. Creep properties

Figs. 12 and 13 show that the threshold stress (and thus the creep resistance) initially increases with increasing $\langle R \rangle$ for both Al–Sc–RE alloys, but decreases for larger radii. A similar effect was observed for Al–Sc alloys [1], Al–Sc–Zr alloys [65], Al–0.06 Sc–0.06 Ti [31] and Al–Sc–RE alloys [54,95]. The initial increase in σ_{th} is due to the additional elastic interactions between the coherent precipitates and the dislocations climbing over the precipitates [43], while the decrease for the largest precipitates is due to the decrease in orowan stress resulting from the reduction in N_v and increase in interprecipitate spacing.

The σ_{th} values for the Al–0.06 Sc–0.02RE and Al–0.06 Sc–0.005RE alloys are larger than in the previously studied Al–Sc or Al–Sc–X alloys with similar volume fractions. For an Al–0.06 Sc alloy at 300 °C [1], the threshold stresses are 8 and 19 MPa for $\langle R \rangle = 4.1$ and 8.5 nm, respectively. The threshold stress for Al–0.07 Sc–0.02Zr alloy with $\langle R \rangle = 8.7$ nm is measured to be 20 MPa [65]. Thus, larger values of ϕ are needed in

Table 2
Different methods used to determine the diffusivity of Yb in Al, D_{Yb} at 300 °C.

Method	D_{Yb} (m^2 s^{-1})	Comments
Coarsening data for 24 h or longer, Al–Sc–Yb	$(5 \pm 4) \times 10^{-21}$	Assuming system has reached the coarsening stage for the Yb-rich precipitates
Incubation time of metastable distribution of sub-critical nuclei, Al–Sc–Yb	$(1.4 \pm 1.7) \times 10^{-19}$	Using approach from Ref. [96]
Coarsening data between 5 and 15 min, Al–Sc–Yb	$(1.6 \pm 0.8) \times 10^{-18}$	Some Sc is diffusing to the precipitates during this period
Diffusion distance measurement, Al–Sc–Yb	$(3.6 \pm 2.9) \times 10^{-19}$	Distance atoms have to travel to form a cluster
Coarsening data, Al–Yb	$(5.7 \pm 1.9) \times 10^{-17}$	Ref. [42]

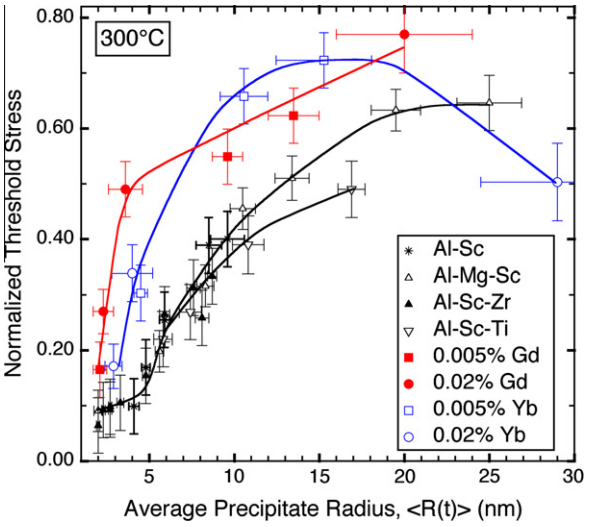

Fig. 15. Threshold stress, σ_{th}, normalized by the Orowan stress $\Delta\sigma_{or}$ for four Al–Sc–RE (50 and 200 ppm Yb or Gd) alloys vs average precipitate radius $\langle R\rangle$ for creep at 300 °C. Data compared with those of Al–Sc [1], Al–Sc–Zr [65], Al–Mg–Sc [10], Al–Sc–Ti [31] and Al–0.06Sc–0.005 RE (RE = Yb or Gd) [54] alloys.

the RE-free alloys to attain similar threshold stresses. Threshold stresses for the Al–0.12 Sc alloy are in the range 14–22 MPa for $\langle R\rangle = 3.0$–5.8 nm [1]. This alloy has larger volume fractions, ranging from 0.46% to 0.49%, depending on the aging temperature, compared with $\phi = 0.28$–0.33% for the present alloys. For the Al–0.18Sc alloy with $\phi = 0.71$–0.75, the threshold stresses are even larger [1], ranging from 17 to 32 MPa for precipitates with $\langle R\rangle = 1.4$–9.6 nm. Fig. 15 displays the threshold stress normalized by the Orowan stress, which normalizes the volume fraction. The RE-containing alloys (50 and 200 at.ppm of Yb or Gd) have significantly higher threshold stresses than the Al–Sc alloys not containing Yb or Gd. Therefore, 200 at.ppm of RE leads to the same increase in threshold stress as 600–1200 at.ppm of Sc.

The remarkable increase in σ_{th} (Figs. 12 and 13) displayed by the Al–Sc–RE alloys, both in the present study and in Refs. [54,95], is probably due to the increased lattice parameter mismatch between the α-Al matrix and the $Al_3(Sc_{1-x}RE_x)$ precipitates [35,36] compared with Al_3Sc, $Al_3(Sc_{1-x}Zr_x)$ [14] or $Al_3(Sc_{1-x}Ti_x)$ [14]. An increased lattice parameter mismatch results in an increase in elastic interactions between lattice dislocations and the precipitates that they bypass by climb, resulting in a higher value of the normalized σ_{th}.

5. Conclusions

The kinetic pathways for the formation of nanosize precipitates in supersaturated Al–0.06 Sc–0.02Yb and Al–0.06 Sc–0.02Gd (at.%) alloys are studied at an aging temperature of 300 °C for times up to 1536 h (64 days), using Vickers microhardness, LEAP tomography and TEM. The conclusions are as follows:

1. Vickers microhardness measurements demonstrate that additions of 0.02% Yb or Gd to Al–0.06 Sc alloys significantly increase the microhardness values of these alloys with respect to the peak hardness of Al–0.06 Sc. The peak α′-precipitate ($L1_2$ structure) number densities N_v of the ternary alloys are $(5.25 \pm 0.55) \times 10^{22}$ and $(4.1 \pm 0.44) \times 10^{22}\,m^{-3}$ for Al–Sc–Yb and Al–Sc–Gd, respectively, which are greater than for Al–0.06 Sc, $(9.33 \pm 2.0) \times 10^{20}\,m^{-3}$. In addition, there is an increase in the volume fraction ϕ of α′-precipitates, owing to the presence of the RE elements. An Al–0.08 Sc alloy has a peak microhardness equal to that of Al–Sc–Yb and slightly larger than that of Al–Sc–Gd.
2. The ternary alloys are in a quasi-stationary state, since ϕ for both alloys is increasing slightly with increasing aging time (Fig. 5). In addition, the slope of the product of N_v and aging t vs t is slowly approaching a value of zero at 384 h (16 day) of aging, indicating that both alloys are not in a stationary state, but rather a quasi-stationary state, before this time.
3. The coarsening rates of Al–Sc–Gd and Al–Sc–Yb are decreased slightly compared with binary Al–Sc alloys, as evidenced by the small time exponents for the evolution of $\langle R\rangle$, N_v and ΔC_i^{α}. The retarding effect of Yb and Gd on precipitate coarsening is, however, significantly less marked than for Zr or Ti.
4. In the Al–Sc–Yb alloy, $Al_3(Yb_{1-x}Sc_x)$ precipitates initially contain overall more Yb than Sc. The Sc concentration in the precipitates increases with increasing aging time, resulting in a Yb-rich core and an enveloping Sc-rich shell structure (Figs. 7, 9 and 10). The Yb and Sc also inter-diffuse during aging, leading to a more uniform concentration throughout the precipitates. The Yb/Sc atomic concentration ratio achieves a value of 0.25 after 96 h (4 days) of aging, thus making Yb a good candidate for replacing a fraction of the more expensive Sc.
5. In Al–Sc–Gd, $Al_3(Sc_{1-x}Gd_x)$($L1_2$ structure) α′-precipitates form with a small fraction of Gd ($x < 0.12$). The relative interfacial Gibbsian excess of Sc at the α-Al/$Al_3(Sc_{1-x}Gd_x)$ interface and the Sc/Gd atomic concentration ratio in the α′-precipitates remain constant between 24 (1 day) and 1536 h (64 day) of aging at 300 °C. Since Gd has a smaller substitution fraction in the α′-precipitates compared with Yb, Gd is not as good a candidate as a ternary addition to Al–Sc alloys as is Yb.
6. The peak-aged Al–Sc–Yb and Al–Sc–Gd alloys exhibit creep resistance at 300 °C, much improved with respect to RE-free Al–Sc, Al–Sc–Ti and Al–Sc–Zr alloys. This confirms the strong effect on creep resistance of lattice parameter mismatch between the α′-precipitates and the α-Al matrix, which is increased by the presence of the Yb or Gd.

Acknowledgements

This research was supported by the United States Department of Energy through Grant DE-FG02–98ER45721. Atom-probe tomographic measurements were performed at the Northwestern University Center for Atom-Probe Tomography (NUCAPT), using a LEAP tomograph purchased with funding from the NSF-MRI (DMR-0420532, Dr. Charles Bouldin, monitor) and ONR-DURIP (N00014-0400798, Dr. Julie Christodoulou, monitor) programs.

References

[1] Marquis EA, Seidman DN, Dunand DC. Acta Mater 2002;50:4021.
[2] Jo HH, Fujikawa SI. Mater Sci Eng A 1993;171:151.
[3] Royset J, Ryum N. Int Mater Rev 2005;50:1.
[4] Hyland RW. Metall Trans A 1992;23A:1947.
[5] Novotny GM, Ardell AJ. Mater Sci Eng A 2001;A318:144.
[6] Tsivoulas D, Robson JD. Mater Sci Forum 2006;519–521:473.
[7] Royset J, Ryum N. Mater Sci Eng A 2005;396:409.
[8] Fuller CB, Seidman DN, Dunand DC. Scripta Mater 1999;40:691.
[9] Fuller CB, Murray JL, Seidman DN. Acta Mater 2005;53:5401.
[10] Marquis EA, Seidman DN, Dunand DC. Acta Mater 2003;51:4751.
[11] Nakayama M, Furuta A, Miura Y. Mater Trans, JIM 1997;38:852.
[12] Marquis EA, Seidman DN. Acta Mater 2001;49:1909.
[13] Iwamura S, Miura Y. Acta Mater 2004;52:591.
[14] Harada Y, Dunand DC. Mater Sci Eng A 2002;329–331:686.
[15] Harada Y, Dunand DC. Scripta Mater 2003;48:219.
[16] Watanabe C, Kondo T, Monzen R. Metall Mater Trans A 2004;35:3003.
[17] Riddle YW, Sanders TH. Metall Mater Trans A 2004;35:341.
[18] Drits MY, Ber LB, Bykov YG, Toropova LS, Anastas'eva GK. Phys Met Metall 1984;57:118.
[19] Krug M, Dunand D, Seidman D. Acta Mater 2011;59:1700.
[20] Fuller CB. Ph.D. thesis. Northwestern University; 2003. <http://arc.nucapt.northwestern.edu/refbase/show.php?record=147>.
[21] Fuller CB, Seidman DN. Acta Mater 2005;53:5415.
[22] Toropova LS, Eskin DG, Kharakterova ML, Dobatkina TV. Advanced aluminum alloys containing scandium. Gordon & Breach; 1998.
[23] Lefebvre W, Danoix F, Hallem H, Forbord B, Bostel A, Marthinsen K. J Alloys Compd 2009;470:107.
[24] Forbord B, Lefebvre W, Danoix F, Hallem H, Marthinsen K. Scripta Mater 2004;51:333.
[25] Knipling KE, Karnesky RA, Dunand DC, Seidman DN. Acta Mater 2010;58:5184.
[26] Knipling K, Seidman DN, Dunand DC. Acta Mater 2011;59:943.
[27] Fujikawa SI. Defect Diffus Forum 1997;143–147:115.
[28] Clouet E, Lae L, Epicier T, Lefebvre W, Nastar M, Deschamps A. Nat Mater 2006;5:482.
[29] Clouet E, Nastar M, Barbu A, Sigli C, Martin G. Solid-solid phase transformations in inorganic materials. TMS; 2005. p. 1.
[30] Tolley A, Radmilovic V, Dahmen U. Scripta Mater 2005;52:621.
[31] Van Dalen ME, Dunand DC, Seidman DN. Acta Mater 2005;53:4225.
[32] Bergner D, Chi NV. Wissenschaftliche Zeitschrift der Padagogischen Hochschule "N.K. Krupskaja". Halle XV, Heft 3; 1977.
[33] Aydinol MK, Bor AS. J Mater Sci 1994;29:15.
[34] Knipling KE, Dunand DC, Seidman DN. Z Metallkd 2006;97:246.
[35] Zalutskaya OI, Kontseyoy VG, Karamishev NI, Ryabov VR, Zalutskii II. Dopovidi Akademii Nauk Ukr. RSR; 1970. p. 751.
[36] Palenzona AJ. J Less-Common Metals 1972;29:289.
[37] Harada Y, Dunand DC. Intermetallics 2009;17:17.
[38] Zalutskaya OI, Ryabov VG, Zalutskii II. Dopovidi Akademii Nauk Ukr. RSR; 1969. p. 255.
[39] Petzow G, Effenberg G. Ternary alloys. Materials Park (OH): ASM International; 1988.
[40] Horovotz CT, Gschneider KA, Melson GA, Youngblood DH, Schock HH. Scandium: its occurence, chemistry, physics, metallurgy, biology and technology. London: Academic Press; 1975.
[41] Mondolfo LF. Aluminum alloys: structure and properties. London: Butterworths; 1976.
[42] Van Dalen ME, Karnesky RA, Cabotaje JR, Dunand DC, Seidman DN. Acta Mater 2009;57:4081.
[43] Marquis EA, Dunand DC. Scripta Mater 2002;47:503.
[44] Kononenko VI, Golubev SV. Russ Metall 1990;2:197.
[45] Sawtell RR, Morris JW. In: Proc of dispersion strengthened aluminum alloys; 1988. p. 409.
[46] Fang H, Chen K, Zhang Z, Zhu C. Trans Nonferrous Metal Soc China 2008;18:28.
[47] Fu J, Nie Z, Jin T, Zou J, Zuo T. J Rare Earths 2005;23:430.
[48] Nie Z, Jin T, Fu J, Xu G, Yang J, Zhou J, et al. Mater Sci Forum 2002;396–402:1731.
[49] Nie Z, Jin T, Zou J, Fu J, Yang J, Zuo T. Trans Nonferrous Metal Soc China 2003;13:509.
[50] Nie ZR, Fu JB, Zou JX, Jin TN, Yang JJ, Xu GF, et al. Mater Sci Forum 2004;28.
[51] Jiang F, Yin Z, Huang B, He Y, Chen S. J Rare Earths 2004;22:600.
[52] Song M, Wu Z, He Y. Mater Sci Eng A 2008;497:519.
[53] Karnesky RA, Van Dalen ME, Dunand DC, Seidman DN. Scripta Mater 2006;55:437.
[54] Van Dalen ME, Dunand DC, Seidman DN. J Mater Sci 2006;41:7814.
[55] Karnesky RA, Dunand DC, Seidman DN. Acta Mater 2009;57:4022.
[56] Krug ME, Werber A, Dunand DC, Seidman DN. Acta Mater 2010;58:134.
[57] Monachon C, Dunand DC, Seidman DN. Small 2010;6:1728.
[58] Massalski. Binary alloy phase diagrams. ASM Int.; 1990.
[59] Meng FG, Zhang LG, Liu HS, Liu LB, Jin ZP. J Alloys Compd 2008;452:279.
[60] Kelly TF, Miller MK. Rev Sci Instrum 2007;78:031101.
[61] Seidman DN. Annu Rev Mater Res 2007;37:127.
[62] Bajikar SS, Larson DJ, Kelly TF, Camus PP. Ultramicroscopy 1996;65:119.
[63] Hellman OC, Vandenbroucke JA, Rüsing J, Isheim D, Seidman DN. Microsc Microanal 2000;6:437.
[64] Hellman OC, Vandenbroucke J, Blatz du Rivage J, Seidman DN. Mater Sci Eng A 2002;327:29.
[65] Fuller CB, Seidman DN, Dunand DC. Acta Mater 2003;51:4803.
[66] Knipling K, Dunand DC, Seidman DN. Microsc Microanal 2007;13:503.
[67] Goodman SR, Brenner SS, Low Jr JR. Metall Trans 1973;4:2363.
[68] Goodman SR, Brenner SS, Low Jr JR. Metall Trans 1973;4:2371.
[69] Defay R, Prigogine I, Bellemans A. Surface tension and absorption. New York (NY): Wiley; 1966.
[70] Dregia SA, Wynblatt P. Acta Metall Mater 1991;39:771.
[71] Cadek J. Creep in metallic materials. New York: Elsevier; 1988.
[72] Frost HJ, Ashby MF. Deformation-mechanism maps: the plasticity and creep of metals and ceramics. Oxford: Pergamon; 1982.
[73] Lagneborg R, Bergman B. Metal Sci 1976;10:20.
[74] Buschow KHJ. J Less-Common Metals 1965;9:452.
[75] Tabor D. Br J Appl Phys 1956;7:159.
[76] Lifshitz IM, Slyozov VV. J Phys Chem Solids 1961;19:35.
[77] Wagner C. Z Elektrochem 1961;65:581.
[78] Ratke L, Voorhees PW. Growth and coarsening. Berlin: Springer; 2002.
[79] Umantsev A, Olson GB. Scripta Metall Mater 1993;29:1135.
[80] Kuehmann CJ, Voorhees PW. Metall Mater Trans A 1996;27A:937.
[81] Calderon HA, Voorhees PW, Murray JL, Kostorz G. Acta Metall Mater 1994;42:991.
[82] Schmuck C, Caron P, Hauet A, Blavette D. Philos Mag A 1997;76:527.
[83] Pareige-Schmuck C, Soisson F, Blavette D. Mater Sci Eng A 1998;250:99.
[84] Pareige C, Soisson F, Martin G, Blavette D. Acta Mater 1999;47:1889.

[85] Sudbrack CK, Yoon KE, Noebe RD, Seidman DN. Acta Mater 2006;54:3199.
[86] Sudbrack CK, Noebe RD, Seidman DN. Acta Mater 2007;55:119.
[87] Marquis EA, Seidman DN. Acta Mater 2005;53:4259.
[88] Ardell AJ. Interface Sci 1995;3:119.
[89] van Dalen ME. Microstructure and creep properties of Al–Sc alloys micro-alloyed with lanthanides (Yb or Gd) and transition metals (Ti or Zr). PhD thesis. Northwestern University; 2007. <http://arc.nucapt.northwestern.edu/refbase/show.php?record=9848>.
[90] Shewmon PG. Diffusion in solids. New York: McGraw-Hill; 1963.
[91] Mao Z, Sudbrack CK, Yoon KE, Martin G, Seidman DN. Nat Mater 2007;6:210.
[92] Asta M, Foiles SM, Quong AA. Phys Rev B 1998;57:11265.
[93] Watanabe C, Watanabe D, Monzen R. Mater Trans 2006;47:2285.
[94] Mao Z. unpublished results 2011.
[95] Karnesky RA, Seidman DN, Dunand DC. Mater Sci Forum 2006;519–521:1035.
[96] Xiao SQ, Haasen P. Acta Metall Mater 1991;39:651.